Article

Climate simulations and ice core data highlight the Holocene conundrum over tropical mountains

Check for updates

Yuntao Bao [1,2] ✉, Zhengyu Liu [1,2], Lonnie G. Thompson [2,3], Ellen Mosley-Thompson[1,2], Lingfeng Wan[4] & Jiuyou Lu [5]

Resolving discrepancies in long-term Holocene temperature trends between climate models and proxy records is essential to improve future climate projections. However, uncertainties in paleoclimate reconstructions limit their ability to constrain models. This study compares ice core-derived oxygen isotope records with isotope-enabled climate simulations to evaluate model performance and investigate Holocene temperature variability. Our results show that simulated and observed oxygen isotope trends in Greenland and West Antarctica are generally consistent, driven by orbital forcing. However, the model underestimates the early Holocene peak and subsequent decline observed in Greenland records. The most striking mismatch appears in tropical mountains, where the model shows a slight increase in isotopic trends, while proxy records indicate a clear decline. The mechanisms controlling this decreasing isotopic trend remain unclear and cannot be fully explained by temperature or hydroclimate changes alone. Addressing this tropical mountain oxygen isotope conundrum requires efforts to improve the model and paleoclimate interpretations.

The Holocene (11 ~ 0 ka before the present) is the latest interglacial period characterized by a relatively stable and warm climate compared to that of the preceding deglaciation (20 ~ 11 ka). Despite the relatively smaller magnitude of climate change in the Holocene compared to the deglaciation, the understanding of Holocene climate evolution still poses significant challenges. A key issue arises from the contrasting temperature trends in the global mean surface temperature (GMST) between paleoclimate proxies and climate models. Temperature reconstructions derived from various sources such as alkenes in ocean sediments, foraminifera Mg/Ca ratio, lake sediments, pollen, ice cores, and speleothems consistently indicate a thermal maximum in the early-to-mid Holocene, when the estimated GMST was approximately 1 °C higher than at present, followed by a gradual cooling from the mid to late Holocene[1,2]. In contrast, the state-of-the-art climate model simulations suggest continuous GMST warming throughout the Holocene with no distinct thermal maximum[3,4]. Model ensembles from the Paleoclimate Model Intercomparison Project (PMIP) estimate a cooling of 0.3 ~ 0.5 °C in the mid-Holocene compared to the present[3,4]. This discrepancy between climate models and proxies, which is referred to as the Holocene temperature conundrum[3], indicates potential uncertainties in both the proxy data and climate models. A portion of

marine sediment and pollen proxies imprint signals to specific seasons associated with organism growth, and thus do not represent the annual mean temperature[5–7]. After removing the seasonal signal from planktic foraminifera records in the tropics using a semi-statistical transformation method, the reconstructed annual mean sea surface temperature (SST) in the tropics, and likely over the globe, exhibits a warming trend throughout the Holocene as suggested by climate models[6], although this transformation method remains in debate[8]. Climate model uncertainties may stem from model resolution, sub-grid parameterization, inaccurate or missed feedback processes such as Arctic sea ice[9], vegetation[10], anthropogenic land use[11], dust[12], and volcanic sulfur emissions[2,13]. Data assimilation by combining proxy records and climate models produces either a weak warming trend[14] or a slight thermal maximum in the mid-Holocene[15]. The discrepancy between models and proxies remains unresolved both globally and regionally, particularly over land areas characterized by spatial heterogeneity. Resolving this discrepancy is critical for increasing the accuracy of future climate model projections.

In this study, we conducted the transient simulation of the Holocene (11 ~ 0 ka) climate using an isotope-enabled earth system model (iTRACE) to rigorously constrain the climate model with paleoclimate tracers and

[1]Department of Geography, The Ohio State University, Columbus, OH, USA. [2]Byrd Polar and Climate Research Center, The Ohio State University, Columbus, OH, USA. [3]School of Earth Sciences, The Ohio State University, Columbus, OH, USA. [4]Frontier Science Center for Deep Ocean Multispheres and Earth System (FDOMES) and Physical Oceanography Laboratory, Ocean University of China, Qingdao, China. [5]Laoshan Laboratory, Qingdao, China. ✉e-mail: bao.291@buckeyemail.osu.edu

better understand Holocene climate variability. The simulated $\delta^{18}O$ in precipitation ($\delta^{18}O_p$) and associated climate variables from iTRACE are then used to drive a forward ice core proxy system model (PSM) PRYSM developed by Dee et al.[16], which simulates $\delta^{18}O$ in ice core ($\delta^{18}O_{ice}$), thereby enabling a direct model-data comparison of $\delta^{18}O_{ice}$ records. Our direct comparison between the modeled and measured $\delta^{18}O_{ice}$ provides a more robust model evaluation with two key advantages: (1) it ensures a fair comparison by weighting iTRACE $\delta^{18}O_p$ with monthly precipitation before driving PRYSM, which mitigates the influence of proxy biases toward specific seasons, and (2) it avoids the need to convert proxy records to temperature, thereby introducing fewer errors. We will focus on $\delta^{18}O_{ice}$ records only from Greenland, Antarctica, and tropical mountains, as glaciers in these regions are sensitive to temperature changes[17,18], and their moisture sources and climate signals are generally clearer and more regionally representative compared to those from mid-latitudes[19]. The representation of $\delta^{18}O_{ice}$ for the in-situ condensation temperature, the so-called temperature effect, has long been confirmed in Greenland and Antarctica[20,21] over different time scales, as well as over tropical mountains during the last deglaciation (20 ~ 11 ka)[17,18,22,23]. This close $\delta^{18}O$-temperature relationship is fundamentally controlled by the Rayleigh distillation process[20]. However, the local temperature signal preserved in $\delta^{18}O_{ice}$ is also modified by changes in moisture source, transportation pathway, precipitation seasonality[24], ice sheet elevation[25], ice flow, and post-deposition processes, including wind-driven redistribution, diffusion, and vapor-snow exchange[26]. These may lead to differences in $\delta^{18}O_{ice}$ trends and may distort the Holocene climate signal over Greenland and Antarctica (Supplementary Notes 1). Nevertheless, consistent $\delta^{18}O_{ice}$ (after removing the effect of ice elevation changes or ice sheet thinning due to ice melting and sea level rise) and borehole temperature signals may still exist over Greenland, with early (8 ~ 9 ka) and the mid-Holocene (5 ~ 6 ka) temperatures that are ~3 °C and 2 ~ 2.5 °C warmer than those in the pre-industrial (PI), respectively[25,27,28]. Carefully selected Antarctic $\delta^{18}O_{ice}$ records show a heterogeneous east-west temperature response in Antarctica (Supplementary Notes 1). A preliminary temperature estimate for Antarctica, utilizing a weighted average from six $\delta^{18}O_{ice}$ records that are biased toward the plateau ice cores, suggests a 1 ~ 2 °C warming during the early Holocene optimum, without a noticeable difference in the mid-Holocene compared to the PI[29].

Tropical mountain ice cores drilled near the ice divide from relatively flat ice caps in the Andes may provide valuable tropical climate signals without being strongly influenced by ice flow[30] and moisture source changes (as the moisture here comes mainly from the upstream Amazon Basin and the equatorial Pacific[18,31–35]). More interestingly, the evolution of proxy $\delta^{18}O_{ice}$ records from Kilimanjaro and Huascarán largely resembles those from sites peripheral to Greenland (e.g., Agassiz and Renland), even quantitatively. The $\delta^{18}O_{ice}$ values from Renland and Huascarán exhibit a decrease of 1.5‰ and 2.1‰, respectively (Fig. 1j and n; Table 1), possibly indicating a dynamically uniform temperature response in the tropical upper troposphere and the polar lower troposphere. If tropical mountain $\delta^{18}O_{ice}$ represents the in-situ temperature change, as is the case for the deglaciation period[18,23], the isotopic depletion in $\delta^{18}O_{ice}$ may suggest a cooling trend from the early to the late Holocene. This seems to be supported by the ice cap advance (and cooling) from the mid (~7ka) to late Holocene inferred from buried rooted plants collected from Quelccaya (14°S) ice margin[36]. However, the carbonate clumped isotopes (Δ_{47}) from Lake Junin, Pumacocha, and Mehcocha (~11 °S) suggest that carbonate formation temperatures were relatively constant (as opposed to a cooling trend) throughout the Holocene compared to the present, though these estimates come with relatively large uncertainties (over ± 2 °C)[37]. When combining temperature estimates from the Amazon basin[38] and the Andean foothills[39], it appears that relatively stable Holocene temperatures might be a coherent feature across the tropical South America region. The apparent divergent proxy temperature estimates highlight an ongoing debate regarding the interpretations of tropical mountain $\delta^{18}O_{ice}$ during the Holocene: whether it reflects a temperature change[17,18,23] or reflects hydro-climate changes, including precipitation, upstream moisture condition, or

monsoon intensity. The latter are inferred mostly from lacustrine sediments or speleothem records[37,40–45]. Further investigation is required to clarify the interpretations of stable water isotopes retrieved from ice core proxies, with the aid of climate model simulations.

For the background information, the features of $\delta^{18}O_{ice}$ during the Holocene, based on a compilation of ice core records from Greenland, Antarctica, and tropical mountains, are thoroughly discussed in Supplementary Notes 1. Then, we present the direct model-proxy data comparison of $\delta^{18}O_{ice}$ at different ice core sites and then discuss temperature change throughout the Holocene. We show that when compared to most Greenland proxy $\delta^{18}O_{ice}$ records, the model simulates a weaker early Holocene maximum and a weaker decreasing trend in $\delta^{18}O_p$ and $\delta^{18}O_{ice}$ in the mid-to-late Holocene. Surprisingly, the model shows an opposite trend when compared to the $\delta^{18}O_{ice}$ records from equatorial mountains throughout the Holocene. This discrepancy highlights the Holocene $\delta^{18}O$ conundrum over the tropical mountains. We propose several hypotheses regarding the forcing mechanisms of the Holocene $\delta^{18}O_{ice}$ changes and discuss possible model deficiencies that may explain the model-data inconsistency.

Results and Discussion
Ice core $\delta^{18}O$ and temperature evolution in the iTRACE model
As the iTRACE model does not account for post-depositional processes in ice cores, we further utilize its output to drive a forward ice core PSM (see Methods). This enables a direct comparison between the model-derived $\delta^{18}O_{ice}$ and the proxy-derived $\delta^{18}O_{ice}$ at each ice core site. Notably, the model $\delta^{18}O_{ice}$ reflects the signal for precipitation-only events. To ensure a consistent comparison, the model surface temperature is also weighted by monthly precipitation. Our comparison and analysis will focus mainly on the variability (considering anomalies rather than absolute values) in $\delta^{18}O_{ice}$ over millennial and longer time scales. Therefore, we perform multi-channel singular spectrum analysis (MSSA) on time series from all ice core sites and examine the leading reconstruction component of the MSSA, which captures the mode of the long-term trend through the Holocene (see Methods).

Greenland. Across all Greenland ice core sites, the model $\delta^{18}O_{ice}$ shows a synchronous evolution with $\delta^{18}O_{ice}$ increases from the early-to-mid Holocene (10 to 7 ka), followed by stable or slight decrease from the mid-to-late Holocene (Fig. 1g-l: blue lines), with a weak $\delta^{18}O_{ice}$ peak in the mid-Holocene (7 ~ 6 ka) compared to the proxies, except at Agassiz and Penny. The $\delta^{18}O_{ice}$ evolution is a response to boreal summer and annual insolation change (Fig. 1a and b), which slightly increase in the early Holocene and then decrease in the mid-to-late Holocene due to the changing precession from boreal summer to winter. In comparison with proxies, model $\delta^{18}O_{ice}$ shows three main discrepancies. First, the model $\delta^{18}O_{ice}$ evolves almost synchronously across all Greenland sites, while proxies show rather asynchronous responses based on the geographical features of the location (Supplementary Notes 1). Second, the magnitude of the Holocene peak in the early-to-mid Holocene (i.e., $\delta^{18}O_{ice}$ response between the peak stage and PI) is weaker by a factor of 2 ~ 4 at most sites (Fig. 1g-l; Table 1), except on Agassiz and Penny where the response of model $\delta^{18}O_{ice}$ magnitude is comparable to that of proxies. During the mid-to-late Holocene, the correlation coefficient of $\delta^{18}O_{ice}$ between the model and proxies ranges from 0.2 to 0.7 (Table 1), indicating a moderate model-data agreement. Third, the model $\delta^{18}O_{ice}$ reaches its maximum approximately 2 ka later than that of proxies at most sites (Fig. 1g–l; Table 1). The relatively weak $\delta^{18}O_{ice}$ peak and synchronous evolution in the model, compared to proxies, may be explained by the absence of certain local feedbacks (e.g., moisture conditions and vertical lapse rate[46]) and smoother topography in the Greenland region due to coarse model resolution, which may result in a more uniform climate response. The relatively late model $\delta^{18}O_{ice}$ peak in the early-to-mid Holocene can be partially attributed to the overestimation of the response of Atlantic Meridional Overturning Circulation (AMOC) to meltwater forcing in the model[47], which produces weaker and slower warming during the early Holocene in high latitudes. Additionally, the model $\delta^{18}O_{ice}$ exhibits two

cycles of centennial variability (observed in both $\delta^{18}O_{ice}$ and temperature) after the 8.2 ka event. These variations align with large-amplitude changes in model AMOC during 8.2 ~ 7.5 ka that are not evident in the $^{231}Pa/^{230}Th$-derived AMOC intensity (Fig. 1e). Consequently, these centennial-scale variations are likely unrealistic and may result from an inadequate meltwater scheme in the simulation. However, this limitation does not significantly impact our discussion of the long-term trend.

The leading mode of the MSSA suggests that the model arithmetic annual mean surface temperature (T_s^{uw}: unbiased 12-month average, as opposed to an annual mean weighted by precipitation amount, which we introduce later) overall follows the model $\delta^{18}O_{ice}$ with a warming trend during the early-to-mid Holocene and a stable or weak cooling trend during the late Holocene at most Greenland sites (Fig. 2a1-a6). However, the evolution of T_s^{uw} is slightly divergent from that of $\delta^{18}O_{ice}$ (Fig. 2a1-a6: blue
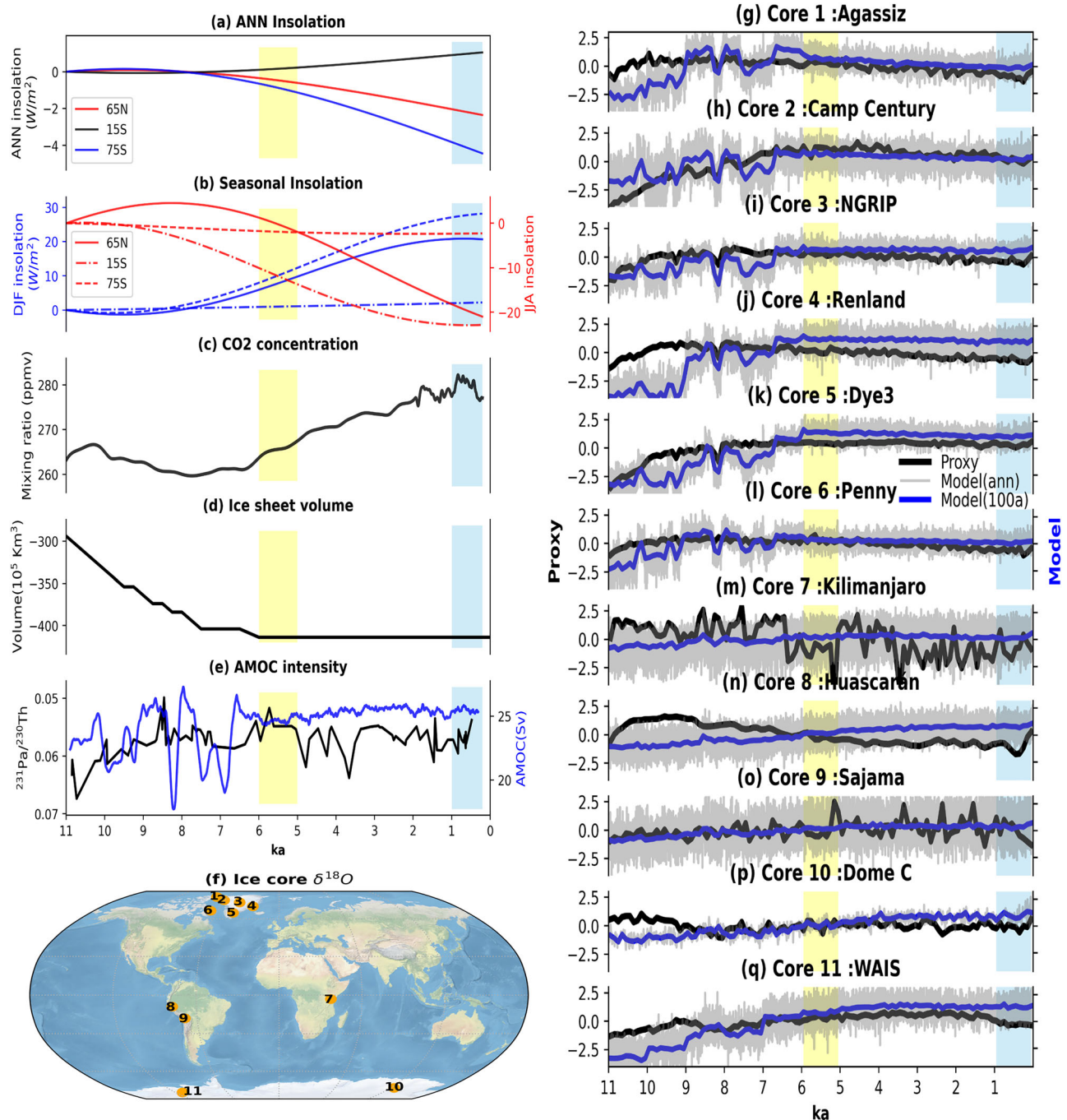
Fig. 1 | Evolution of model and proxy $\delta^{18}O_{ice}$ during the Holocene. a Annual mean orbital-induced solar insolation forcing (W/m²) at 65°N (red), 15°S (black), and 75°S (blue); (**b**) Orbital-induced insolation forcing (W/m²) at 65°N (solid lines), 15°S (dash dotted lines), and 75°S (dashed lines) in DJF (blue; left axis) and JJA (red; right axis); (**c**) Global mean atmospheric CO_2 concentration (ppm); **d** Global ice volume change (10⁵ km³) relative to the Last Glacial Maximum; **e**$^{231}Pa/^{230}Th$ reconstructed from sediment core GGC5 as a proxy for AMOC intensity (black) and model AMOC intensity (blue); **f** Geographical location of ice cores used in this study; (**g-q**) Time series of proxy $\delta^{18}O_{ice}$ averaged over 100-year bins (‰; black), model annual $\delta^{18}O_{ice}$ (‰; gray), and model $\delta^{18}O_{ice}$ averaged over 100-year bins (‰; blue) from: (**g**) Agassiz[94]; (**h**) Camp Century[95]; (**i**) NGRIP[96], (**j**) Renland[94], (**k**) Dye 3[96], (**l**) Penny[97], (**m**) Kilimanjaro[98], (**n**) Huascarán[23], (**o**) Sajama[22], (**p**) Dome C[99], and (**q**) WAIS David[54]. The yellow and blue filled shadings denote the mid-Holocene and PI, respectively. Solar insolation values in (**a**) and (**b**) are the differences respective to 11 ka.

Table 1 | The timing of the maximum $\delta^{18}O_{ice}$ value (peak year) and the response of $\delta^{18}O_{ice}$ between the peak time in the Holocene and the present-day ($\triangle\delta^{18}O_{ice}$), derived from the ice core proxies and the model

Ice core site	$\delta^{18}O_{ice}$ Peak year (ka)		$\triangle\delta^{18}O_{ice}$: Peak year-PI (‰)		$\delta^{18}O_{ice}$ correlation between the proxy and model (6.5~0ka; N = 66)
	Ice core	Model	Ice core	Model	
Agassiz	7.8	6.6	1.63	1.75	0.72 (p = 0.04; df = 12)
Camp Century	4.5	6.6	1.24	0.71	0.65 (p = 0.001; df = 20)
NGRIP	7.8	6.0	1.07	0.17	0.18 (p = 0.17; df = 52)
Renland	7.8	6.0	1.54	0.37	0.45 (p = 0.004; df = 38)
Dye 3	stable	5.9	stable	0.45	0.25 (p = 0.17; df = 31)
Penny	8.0	8.0	1.26	0.98	0.64 (p = 0.003; df = 17)
Kilimanjaro	8.0	4.8	2.03	0.37	0.01 (p = 0.95; df = 55)
Huascarán	9.5	0	2.16	+	−0.8 (p = 0.04; df = 6)
Sajama	stable	stable	stable	stable	0.03 (p = 0.84; df = 56)
Dome C	10.0	0	0.76	+	0.07 (p = 0.67; df = 37)
WAIS	2 ~ 4	0 ~ 4	0.93	+	0.41 (p = 0.14; df = 12)

Also shown are the correlation coefficients of $\delta^{18}O_{ice}$ between the ice core proxy and the model during 6.5 ~ 0 ka. Each time series contains 66 data points. Values within the parenthesis are statistical p-values and the effective number of degrees of freedom (df), which account for the influence of autocorrelations on the estimation of significance levels for the correlation coefficients.
Time series of $\delta^{18}O_{ice}$ without a noticeable Holocene maximum are marked as "stable". Time series with a gradually increasing trend throughout the entire Holocene period are marked as '+'.

and solid orange lines) since the model annual T_s^{uw} mainly follows the boreal winter temperature. We note that model $\delta^{18}O_{ice}$ is a footprint of temperature associated with precipitation events, and therefore, the seasonal cycle of precipitation should be considered for a fair comparison of Holocene temperature change. Model annual surface temperature weighted by precipitation ($T_s^{p_w}$) exhibits an evolution closer to $\delta^{18}O_{ice}$ compared to that of T_s^{uw}, consistent with the isotopic temperature effect. This is also clear in a larger temporal slope of model $\delta^{18}O_p$ against $T_s^{p_w}$ ($\delta^{18}O_p/T_s^{p_w}$) compared to $\delta^{18}O_p/T_s^{uw}$ at all Greenland sites in the Holocene (Fig. S1e-f. Supplementary Notes 2). Our results are consistent with Werner et al.[48], highlighting the importance of the precipitation seasonality in explaining the discrepancy between borehole (unbiased) and isotope-inferred (biased) temperature. Existing proxy $\delta^{18}O_{ice}$ and borehole temperature reconstructions suggest an early Holocene warming of 2 ~ 3 °C over the Greenland ice sheet and ~4 °C over the Agassiz ice cap[25,27,28,49,50]. For comparison, model T_s^{uw} generally contrasts with the temperature reconstructions. In contrast, model $T_s^{p_w}$ exhibits early Holocene warming at all ice core sites, with a Holocene Thermal Maximum (HTM) ranging from 0.12 to 3.52 °C and an average of 1.0 °C, which is overall weaker than observations by a factor of 2. The underestimation of the model temperature response over Greenland could be attributed to the model's weak sensitivity to orbital-induced insolation forcing[3].

Antarctica. The model partially reproduces the evolution of Antarctic $\delta^{18}O_{ice}$ throughout the Holocene. The model $\delta^{18}O_{ice}$ for Dome C in the East Antarctic shows a gradual isotopic enrichment in the early-to-mid Holocene and then a stabilization in the late Holocene (Fig. 1p: blue line; Table 1). In contrast, proxy $\delta^{18}O_{ice}$ reaches its maxima in the early Holocene (11 ~ 9 ka), followed by a decrease during 9 ~ 7 ka (Fig. 1p: black line). The early Holocene maxima in the proxy is partially attributed to changes in $\delta^{18}O$ in ocean surface waters ($\delta^{18}O_{sw}$) due to decreasing ice sheet volume during the final deglaciation and the gradually intensified AMOC (Fig. 1e: black line) removed heat from the high southern latitudes[51]. The model $\delta^{18}O_{ice}$ does not produce the early Holocene maxima at Dome C, probably due to inaccurate boundary conditions and a biased model response to ice volume and meltwater forcing. For the WAIS Divide in West Antarctica, the model reproduces an increase in $\delta^{18}O_{ice}$ as suggested by the proxy in the early-to-mid Holocene (Fig. 1q) but shows a mismatch in the late Holocene when model $\delta^{18}O_{ice}$ value continues to increase while $\delta^{18}O_{ice}$ first stabilizes and then decreases. This may be explained by model bias in response to local insolation change, a point that will be discussed later in this section.

Unlike in Greenland, where the seasonality of precipitation is important in driving annual $\delta^{18}O_{ice}$ and temperature evolution, the influence of precipitation seasonality in Antarctica is negligible[48,52]. This is seen in the close resemblance of model $\delta^{18}O_{ice}$ evolutions among different seasons (Fig. 2 b10-b11) and the similarity in model annual T_s^{uw} and $T_s^{p_w}$ evolutions (Fig. 2 a10-a11: comparing dashed and solid orange lines). Thus, only T_s^{uw} is used when referring to surface temperature in Antarctica. The model T_s^{uw} follows $\delta^{18}O_{ice}$ throughout the Holocene, with a gradual warming in the early-to-mid Holocene and a warming hiatus in the late Holocene. A compilation of proxy $\delta^{18}O_{ice}$ from the East Antarctica plateau and coast suggests an HTM (11 ~ 9 ka) of ~1 °C compared to the PI climate (Supplementary Notes 2), while no discernible change is evident in the mid-Holocene[29] (red line in Fig. S2b). In contrast, our model shows a continuous warming of 1.7 °C from 11 to 3 ka and a missing HTM at Dome C (Fig. 2a10: orange lines; Fig. S2b), driven by increased DJF insolation and CO_2 concentration. For West Antarctica, independent borehole temperature records from the WAIS Divide[53] (red line in Fig. S2c) suggest a gradual warming from 8 to 3.5 ka, reaching a steady thermal maximum of ~1.5 °C (compared to the PI) and ~1 °C cooling after 1.5 ka. The high-resolution seasonal temperature derived from the WAIS Divide calibrated isotope records[54] indicates a dominant role of summer on the annual mean temperature during the mid-to-late Holocene (comparing orange and red lines in Fig. S2c), likely driven by local maximum insolation in December (green line in Fig. S2a)[54]. For comparison, our model also exhibits a weak thermal maximum (offset 1 ka to 9 ~ 8 ka) followed by a comparable warming (1 ~ 1.5 °C) from 8 to 3.5 ka and then a warming hiatus in the late Holocene (Fig. 2a11: orange lines; Fig. S2c), driven by increased mean DJF insolation during the mid-to-late Holocene.

Tropical Mountains. Direct model-data comparisons of $\delta^{18}O_{ice}$ over tropical high mountains are challenging because the coarse model resolution cannot resolve the small-scale isolated high mountain peaks of these ice core sites. However, since the variability of $\delta^{18}O_p$ is highly correlated with and condensed from the environmental vapor $\delta^{18}O$ ($\delta^{18}O_v$)[55], we treat the model $\delta^{18}O_v$ at the height of the ice core site as an approximation of the model $\delta^{18}O_p$, following our recent work[18]. To enable a direct comparison of $\delta^{18}O_{ice}$ between proxy and model at the same altitude, we first establish a linear relationship between the model near-surface $\delta^{18}O_v$ and $\delta^{18}O_p$, as these two are typically in equilibrium. Assuming this linear relationship remains constant with height, we can calculate a pseudo-$\delta^{18}O_p$ at the ice core altitude based on the model $\delta^{18}O_v$. This pseudo-$\delta^{18}O_p$ is then used to force the ice core PSM model,

yielting the final tropical mountain $\delta^{18}O_{ice}$ for direct comparison. Note that the model annual mean $\delta^{18}O_v$ is also weighted by monthly precipitation ($\delta^{18}O_v^{pw}$) at each ice core site to mimic the $\delta^{18}O$ in precipitation ($\delta^{18}O_P$) and, in turn, the $\delta^{18}O_{ice}$. This weighted average approach also accounts for the fact that tropical mountain $\delta^{18}O_{ice}$ signal may be highly biased toward wet seasons, as much of the accumulation occurs during the wet season and the reduction of snow height by sublimation and wind scour tends to modify and remove the dry season signals[31,56–58].
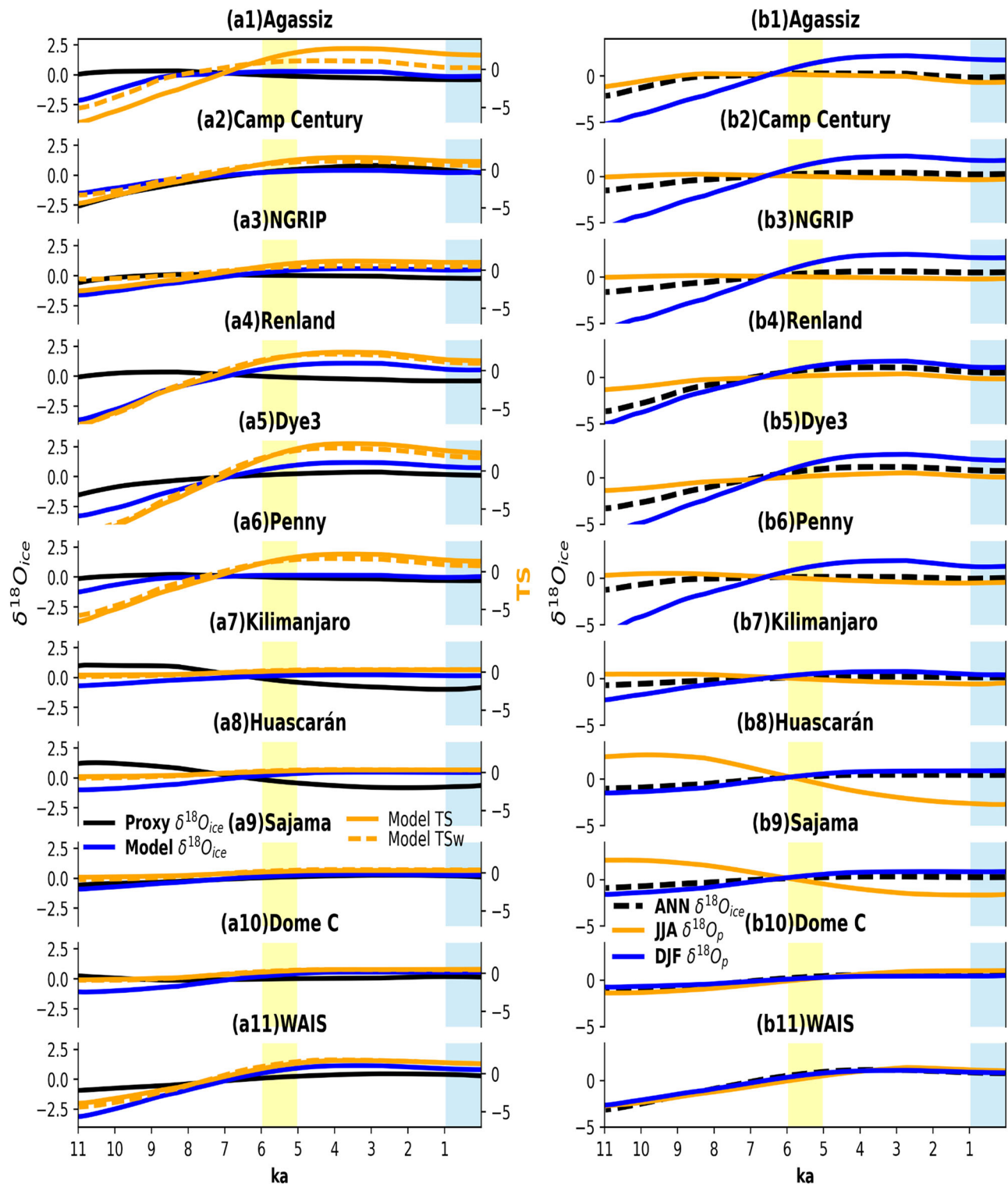

Fig. 2 | Long-term trend of $\delta^{18}O_{ice}$ and temperature for different seasons during the Holocene. The leading reconstruction component (long-term trend) of the MSSA (see Methods) for the time series of annual (**a1-a11**) proxy $\delta^{18}O_{ice}$ (‰; black: left axis), model $\delta^{18}O_{ice}$ (‰; blue: left axis), model temperature (°C; dashed orange lines are for arithmetic annual mean T_s^{uw}; solid orange lines are for annual mean weighted by monthly precipitation T_s^{pw}: right axis). **b1-b11** show the leading reconstruction component of the MSSA for model $\delta^{18}O_P$ during JJA (orange) and DJF (blue). Model annual model $\delta^{18}O_{ice}$ is included for reference (dashed black line, identical to the blue line in **a1-a11**). The eigenvalues, or variance contributions, of the MSSA leading mode are 50% for proxy $\delta^{18}O_{ice}$, 66% for model annual $\delta^{18}O_{ice}$, 71% for model JJA $\delta^{18}O_{ice}$, and 71% model DJF $\delta^{18}O_{ice}$. The geographic location of each ice cores is shown in Fig. 1f.

In contrast to the polar regions, where the model generally reproduces the $\delta^{18}O_{ice}$ evolution observed in proxies, albeit with a much weaker amplitude (Fig. 1; Table 1), the evolutions of model $\delta^{18}O_{ice}$ throughout the Holocene are opposite to that observed in proxies from Kilimanjaro, Huascarán (Fig. 1m and n; Fig. 3c, d), and Illimani[59] (gray line in Fig. 3c, but for δD_{ice}). Specifically, the model $\delta^{18}O_{ice}$ shows an isotopic enrichment of
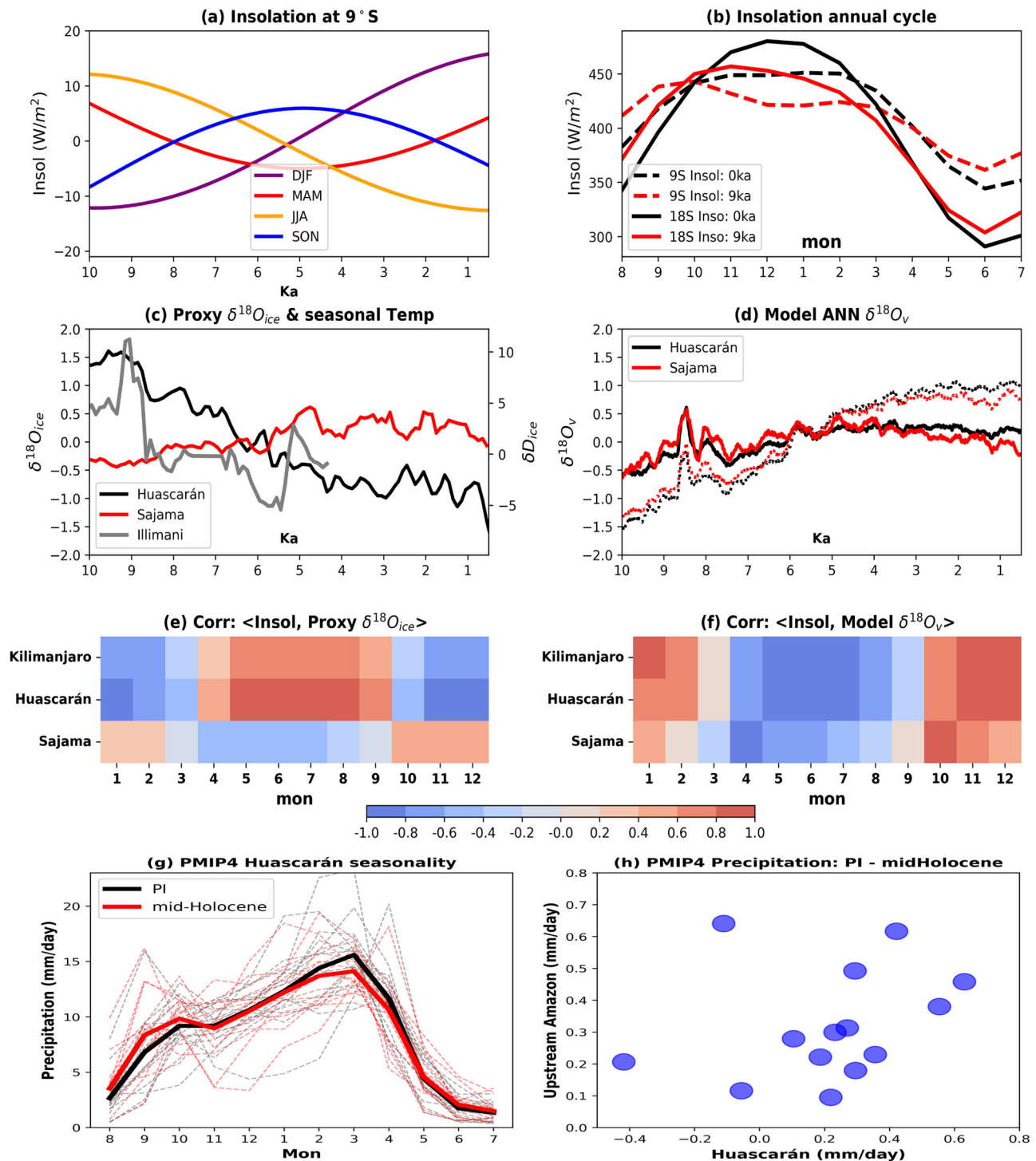
Fig. 3 | Hypothesis testing of the forcing mechanisms driving the $\delta^{18}O_{ice}$ long-term trend during the Holocene. a Time series of seasonal mean solar insolation at 9°S (W m-2). **b** Seasonal cycle of solar insolation at 9°S (Huascarán latitude) for 0 ka (dashed black) and 9 ka (dashed red), and at 20°S (Sajama latitude) for 0 ka (solid black) and 9 ka (solid red). **c** Time series of proxy $\delta^{18}O_{ice}$ records (‰) from Huascarán (black: left axis), Sajama (red: left axis), and δD_{ice} records from Illimani[59] (gray: right axis). **d** Time series of model annual mean $\delta^{18}O_v$ at the ice core altitude of Huascarán (black) and Sajama (red). Solid lines are for the arithmetic annual mean ($\delta^{18}O_v^{uw}$) and dashed lines are the annual mean weighted by monthly precipitation ($\delta^{18}O_v^{pw}$). **e** Correlation coefficient between $\delta^{18}O_{ice}$ and 9°S solar insolation for each month throughout the Holocene at each ice core site. **f** Correlation coefficient between model arithmetic annual mean $\delta^{18}O_v$ and 9°S solar insolation for each month throughout the Holocene. Note that time series in (**a**), (**c**), and (**d**) are shown as anomalies from the climatological mean. **g** Seasonality of precipitation at Huascarán derived from PMIP4-CMIP6 simulations (including the iTRACE) for the mid-Holocene (red) and PI (black). Solid lines are the results of multi-model ensembles, and dashed lines are for each model. **h** Annual precipitation differences (PI minus mid-Holocene) over Huascarán and upstream Amazon region derived from PMIP4-CMIP6 simulations (including the iTRACE). Each dot represents a single model.

$0.8 \sim 1.8‰$ from the early to the late Holocene, while the proxy $\delta^{18}O_{ice}$ exhibits an isotopic depletion of 1.5‰ (Table 1). This is surprising, given that the model is in good agreement with the proxy $\delta^{18}O_{ice}$ at Huascarán during the last deglaciation and is proven to be an indicator of air temperature[18]. Further analysis indicates that the increase in the model annual $\delta^{18}O_{ice}$ is largely driven by its increasing trend during the wet season or DJF (Fig. 2b8), although the dry season (JJA) exhibits a decreasing trend similar to that observed in proxies. Unlike Kilimanjaro and Huascarán, the model $\delta^{18}O_{ice}$ evolution aligns quantitatively with that of Sajama, a near-subtropical ice core, (Fig. 1o), exhibiting a long-term trend similar to $\delta^{18}O_{ice}$ at the WAIS Divide.

The model annual mean temperature (we only discuss T_s^{uw} here given the similarity between T_s^{uw} and T_s^{pw} in the tropics) follows the model annual $\delta^{18}O_{ice}$ at the same altitude, with a gradual warming of ~1.5 °C throughout the Holocene at the three tropical mountain ice core sites (Fig. 2a7-a9), which is comparable to the magnitude of the general upper-troposphere warming in the tropics (Fig. S5a and c). Despite the absence of independent temperature records reconstructed from the ice cores, the warming trend suggested by the iTRACE model does not appear to be supported by limited temperature estimates from lacustrine sediments, derived from either carbonate clumped isotopes[37] or Branched glycerol dialkyl glycerol tetraethers (brGDGTs)[60]. These estimates suggest a likely stable temperature throughout the Holocene, albeit with about ± 2 °C uncertainties. Furthermore, even if $\delta^{18}O_{ice}$ reflects the in-situ temperature change during the Holocene (as is the case during the last deglaciation), one would estimate a $0.8 \sim 1.8$ °C cooling at Kilimanjaro and Huascarán from the early to late Holocene, contrasting with the warming trend suggested by the model. In contrast, an estimated 1.0 °C warming at Sajama would be comparable to the model results (Supplementary Notes 2). Our preliminary analysis reveals the challenges of rigorously estimating Holocene temperature changes and reconciling the differences among various proxies and climate models over the tropical mountains.

The Holocene Conundrum in tropical mountain ice core $\delta^{18}O$

Although the model tends to underestimate the $\delta^{18}O_{ice}$ trend in polar regions, the forcing mechanisms there are relatively straightforward: polar $\delta^{18}O_{ice}$ responds primarily to Holocene insolation forcing through a robust isotopic temperature effect (see above discussions). However, the forcing mechanisms of the isotopic trend observed in tropical mountain $\delta^{18}O_{ice}$ remain unclear and, therefore, pose the Holocene Conundrum in tropical mountain $\delta^{18}O_{ice}$ change. Taking the Huascarán ice core as an example (and similarly for the Illimani ice core), the present-day observations suggest a strong seasonality of precipitation at the Huascarán site (Fig. S3b6; Fig. S4b2), with a single peak from December to March and the corresponding $\delta^{18}O_{ice}$ and $\delta^{18}O_p$ minimum (but offset a month toward April as shown in Fig. S4c2). If we assume the Holocene $\delta^{18}O_{ice}$ is an indicator of annual temperature change dominated by local processes, one should expect a warming trend and an increase in proxy $\delta^{18}O_{ice}$ throughout the Holocene in response to increasing insolation in the wet season (DJF) (Fig. 3a) when perihelion is shifting toward austral summer. This expected warming and $\delta^{18}O_{ice}$ increase are produced in the iTRACE model but are opposite to the $\delta^{18}O_{ice}$ decrease observed in ice core records (Fig. 1n; Fig. 3c, d), raising the puzzle here. A similar case is evident in the Kilimanjaro ice core, where the seasonal cycle of precipitation shows two peaks as the Inter-Tropical Convergence Zone (ITCZ) passes over 3 °S twice a year (Fig. S3b5). Under the same assumptions, we should expect weak warming and an associated $\delta^{18}O_{ice}$ increase in response to a weak increase in wet season insolation (Fig. 3a), as shown in the iTRACE model instead of the long-term decreasing trend observed in Kilimanjaro proxy $\delta^{18}O_{ice}$ (Fig. 1m). Therefore, we raise a key question here: What drives the decrease in $\delta^{18}O_{ice}$ in the near-equator region, as observed in the Huascarán (9 °S), Kilimanjaro (3 °S), and Illimani (16.6 °S) ice cores? Proposing several hypotheses to these questions will be helpful in explaining the model-proxy discrepancy on tropical mountain $\delta^{18}O_{ice}$ evolution throughout the Holocene.

Despite a significant negative correlation ($r < −0.7$; $p < 0.01$) between solar insolation flux and proxy $\delta^{18}O_{ice}$ values during the wet season (DJF) (Fig. 3e), a significant positive correlation ($r > 0.7$; $p < 0.01$) between the two is found from May to September (Fig. 3e) for Kilimanjaro and Huascarán (and also Illimani). This suggests one explanation (Hypothesis I): that the seasonality of precipitation may shift gradually from DJF to JJA or SON throughout the Holocene, assuming proxy $\delta^{18}O_{ice}$ serves as a signal of the local temperature during the wet season. In other words, decreasing SON (or JJA) insolation during the mid-to-late Holocene may drive a decreasing $\delta^{18}O_{ice}$ associated with a cooling trend. This hypothesis seems to be supported by a shift of the insolation maxima from DJF toward SON at 9 °S in the early Holocene compared to the PI (Fig. 3b: comparing black and red dashed lines). Correspondingly, we examine the precipitation seasonality changes over the tropical Andes from iTRACE and PMIP4-CMIP6 models. However, most models indicate minimal changes in the seasonality of precipitation from the mid-Holocene to PI, consistently showing a wet season during DJF (Fig. 3g). Similarly, the seasonality change of the model $\delta^{18}O_v$ over Huascarán is not evident (Fig. S3b6 and c6). This suggests that the temperature signal during the wet season may not be sufficient to explain the Holocene $\delta^{18}O_{ice}$ change observed in proxies. In contrast, the possible mechanism behind the $\delta^{18}O_{ice}$ changes in the Sajama ice core appears to be more straightforward. The insolation seasonality at 20 °S changes less over time (Fig. 3b: comparing black and red solid lines) and the Sajama $\delta^{18}O_{ice}$ may be constantly biased toward DJF (wet season) with an increasing trend due to possible warming in response to increasing insolation (Fig. 3e).

It is crucial to emphasize that the aforementioned hypothesis of seasonality changes (Hypothesis I) refers specifically to the $\delta^{18}O_{ice}$ signal associated with wet season or precipitation events. We also note the importance of the vapor-snow exchange process (mostly through snow sublimation) in post-deposition fractionation (increasing $\delta^{18}O_{ice}$ values) and thus altering the annual mean $\delta^{18}O$ signal, especially in precipitation cessation or intermission periods[26,61,62]. This suggests a second explanation of forcing mechanisms (Hypothesis II) that tropical mountain $\delta^{18}O_{ice}$ may preserve temperature signals not only for the wet season (and precipitation events) but also for the dry season (and precipitation cessation) if the vapor-snow exchange occurs when snow is deposited and metamorphosed into ice. Although this hypothesis cannot be directly corroborated due to the absence of high temporal resolution observations in both $\delta^{18}O_{ice}$ and near-surface $\delta^{18}O_v$, we propose an alternative way to test Hypothesis II, that is, by comparing the proxy $\delta^{18}O_{ice}$ records with model $\delta^{18}O_v$ in arithmetic annual mean ($\delta^{18}O_v^{uw}$). This simple approach includes model $\delta^{18}O_v$ signals from both precipitation events and precipitation intermissions. It's interesting to see that the magnitudes of $\delta^{18}O_v^{uw}$ increase are much weaker than that of $\delta^{18}O_v^{pw}$ throughout the Holocene (and even a weak depletion in the late Holocene is observed: Fig. 3d) because $\delta^{18}O_v^{pw}$ tends to be biased toward the wet season (DJF) when solar insolation increases. The closer similarity between $\delta^{18}O_v^{uw}$ and $\delta^{18}O_{ice}$ throughout the Holocene suggests that climate signals during precipitation intermissions and dry season (when dry season cooling throughout the Holocene is driven by decreasing insolation) are also important in determining the annual $\delta^{18}O_v$ and may influence the final $\delta^{18}O_{ice}$ values. However, it is important to note that strong sublimation or wind scour may remove the snow surface layer containing a dry season signal, as observed on glaciers from Cerro Tapado[56], Sajama[63], and Quelccaya[58]. As a result, $\delta^{18}O_{ice}$ values may be constantly biased toward the wet season. Although detailed observations from field campaigns and snow pit measurements for the Huascarán ice core are not available, instrumental observation from the nearest GNIP (Global Network of Isotopes in Precipitation) site Marcapomacocha (11.4 °S; 4400 m) indicates that over 90% of the annual precipitation falls between October and the following April. Consequently, minimal precipitation during the dry season may lead to significant sublimation and isotopic information loss at the Huascarán ice core location. If this is the case, then Hypothesis II, which incorporates the temperature signal from the dry season, may not be a feasible explanation.

The proposed Hypotheses I and II are based on the assumption of an isotopic temperature effect, which requires a forcing to drive a cooling trend

to explain the decreasing $\delta^{18}O_{ice}$ observed in proxies. However, the expected cooling trend does not seem to be supported by most independent paleo-climate proxies. Additionally, we note significant uncertainties and inconsistencies among the different proxies. For instance, the expansion of the Quelccaya ice cap margin, inferred from the radiocarbon-dated rooted plants, suggests a cooling transition from the mid-Holocene to PI[36], while quantitative temperature reconstructions from lake sediments show a relatively stable temperature throughout the Holocene[37,60]. This implies that different proxies may have different sensitivity to temperature change, warranting further investigations. We also note that the proposed mechanisms—either changes in precipitation seasonality or temperature signals from both dry and wet seasons—may be unrealistic to achieve (as detailed above). Moreover, the relatively smaller magnitude of the tropical temperature response driven by orbital precession during the Holocene, compared to a stronger response driven by CO_2 and ice sheets during the last deglaciation, may result in a relatively stronger tropical precipitation response during the Holocene[64] (Fig. S5a and b). Therefore, the role of precipitation or upstream moisture/monsoon signal in affecting the Holocene $\delta^{18}O_{ice}$ may be important. This suggests a third explanation: that the proxy $\delta^{18}O_{ice}$ may reflect local or upstream hydroclimate signals (Hypothesis III). The decreasing trend in Kilimanjaro, Huascarán, and Illimani $\delta^{18}O_{ice}$ may be explained by a local precipitation increase or depleted incoming $\delta^{18}O_v$ linked to stronger South American Monsoon[41,43,65] (and larger upstream rainout) in response to increasing insolation and stronger convective diabatic heating in the wet season (notably in DJF)[42]. In other words, if Hypothesis III is correct, an increasing trend in precipitation (dominated by wet season) throughout the Holocene over the tropical Andes and/or upstream Amazon basin would be expected. However, we note that the precipitation increase or South American Monsoon intensification seems to have a latitudinal-dependent, time-varying pattern as suggested by multiple independent proxy reconstructions. Specifically, the decrease in coupled calcite and fluid inclusion $\delta^{18}O$ collected from Cueva del Tigre Perdido[42] (at 3 °S), and the significant decrease in authigenic calcite $\delta^{18}O$ observed in lakes Pumacocha and Junin[37,40,44,66] (at 11 °S), began around 9 ~ 10 ka. The water level of Lake Titicaca (at 16 °S) began rising around 6 ka, following a dry period during the early-to-mid Holocene[40,67]. Thus, the proxies suggest large uncertainties in hydroclimate change during the early-to-mid Holocene. In contrast, there is a greater consensus regarding the increase in precipitation over the tropical Andes after the mid-Holocene. This is further supported by the decreasing Huagapo Cave $\delta^{18}O$[37], the advances of the Yanacocha Huagurucho glacier (50 km away from Lake Junin)[68], and the increase of the upstream Amazon humid forests and vegetations implied from pollen records[69]. Despite the complexity of the Holocene hydroclimate, time series patterns of stalagmite and lake carbonate $\delta^{18}O$ are largely consistent with those observed in the Huascarán ice core, even quantitatively.

Our iTRACE model shows an increase in annual mean and wet season precipitation from 7.5 to 3ka for Huascarán (Fig. S6b: blue line). However, the model $\delta^{18}O_{ice}$ at the Huascarán ice core altitude does not exhibit a decreasing trend, as would be expected under the amount effect mechanism. Most climate models from PMIP4-CMIP6 also confirm a noticeable increase in annual precipitation over the tropical Andes (Huascarán) and across the Amazon from the mid-Holocene to PI (Fig. 3h), aligning with observations from paleoclimate proxies discussed above. Nevertheless, since the increased precipitation or intensified South American Monsoon are evident only during the mid-to-late Holocene, this wet trend cannot fully explain the observed rapid decreasing in Huascarán $\delta^{18}O_{ice}$ during the early Holocene (10 ~ 7ka). At present, we are unable to corroborate whether and to what extent changes in hydroclimate contributed to isotopically depleted incoming vapor $\delta^{18}O_v$ and/or local $\delta^{18}O_p$ during the mid-to-late Holocene. In future work, we can incorporate water-tagging code into a high-resolution iTRACE model capable of resolving high mountain topography to further detect the hydrological footprint of Andes $^{18}O_{ice}$ and, thereby better assess the validity of this hypothesis.

Possible model deficiencies

The iTRACE model may have deficiencies in simulating the tropical climate, as evidenced by the $\delta^{18}O_{ice}$ mismatch between the model and data from Kilimanjaro, Huascarán, and Illimani. This model-data discrepancy is unlikely to result from seasonality, as the model well reproduces the seasonality of precipitation, $\delta^{18}O$, and temperature at all GNIP sites in the tropical mountain regions (Fig. S4). Here, we propose three possible deficiencies in the iTRACE model: the coarse model resolution, unrealistic boundary conditions, and poleward energy transport bias. Specifically, the coarse model resolution largely smooths the topography, making it impossible to resolve the high tropical mountains and the corresponding terrain climate effects. The absence of the topographic effect may cause bias in simulating the local response/trend of near surface $\delta^{18}O_v$ and $\delta^{18}O_p$ over the high mountain peaks due to unrealistic condensation processes. Missing sub-grid physics of clouds and precipitation in a coarse model may lead to a weak response in local $\delta^{18}O_p$. In addition, the iTRACE simulation for the Holocene prescribes vegetation based on the PI period instead of using realistic land boundary conditions or coupled dynamic vegetation. The possible low vegetation bias throughout the Holocene may cause relatively reduced convection and moisture recycling over the Amazon basin[70], leading to a positive trend bias in $\delta^{18}O_v$ transported from the Amazon basin to the Andes. In addition, the model lacks consideration of the latitudinal variation of atmospheric methane content that is intricately linked to vegetation changes and may also influence regional temperatures in the tropics. Furthermore, model cold temperature biases in mid-high latitude land areas (particularly in the North Hemisphere) during the early-to-mid Holocene may also contribute to the cold temperature biases over the tropics, thereby explaining part of the positive trend bias in $\delta^{18}O_p$ (and $\delta^{18}O_{ice}$) throughout the Holocene, due to the interconnection of low and high latitudes through atmospheric poleward heat transport (see more details in the follow-up paper). Finally, we note that the ice core PSM we use involves several assumptions and simplifications (see Methods). Additional post-condensation processes, such as sublimation and vapor-snow exchange in snow and firn, could further alter the $\delta^{18}O_{ice}$ values and may impact the direct comparison between the model and ice core records[16,58,71].

Conclusions

In this study, we directly compare $\delta^{18}O_{ice}$ records from Greenland, Antarctica, and the tropical mountains with our isotope-enabled transient simulations of the Holocene climate, using the iCESM model combined with an ice core PSM. This provides valuable insights into Holocene temperature variability and, thereby some implications regarding the Holocene Temperature Conundrum. Our analyses show that:

(1) In response to the boreal summer insolation decrease, an early Holocene maximum in Greenland $\delta^{18}O_{ice}$ is followed by a decreasing trend during the mid-to-late Holocene and a 2 ~ 3 °C cooling, with a temporal slope of 0.3 ~ 0.55‰/ °C. The model simulates a much weaker magnitude of the early Holocene peak in $\delta^{18}O_{ice}$ and the subsequent decreasing trend by a factor of 2 to 4 at most Greenland ice core sites.

(2) Antarctica exhibits a potential west-east heterogeneity in $\delta^{18}O_{ice}$ evolution. Driven by an increase in DJF insolation, the West Antarctica ice core, WAIS Divide, shows a gradual increase in $\delta^{18}O_{ice}$ from 11 ~ 2 ka, corresponding to ~1.5 °C warming estimated from the borehole temperature, with a temporal slope of ~0.8‰/ °C. The model $\delta^{18}O_{ice}$ shows an overall increasing trend throughout the Holocene and partially reproduces the $\delta^{18}O_{ice}$ variability observed in proxies.

(3) Tropical mountain ice cores from Kilimanjaro, Huascarán, and Illimani exhibit $\delta^{18}O_{ice}$ evolution similar to those in Greenland (notably the Renland site), with a ~ 2‰ decrease in proxy $\delta^{18}O_{ice}$ and a possible 0.8 ~ 1.8 °C cooling from the early to the late Holocene, assuming that $\delta^{18}O_{ice}$ serves as a proxy of in-situ temperature. We highlight that the forcing mechanisms driving the decreasing trend in tropical mountain proxy $\delta^{18}O_{ice}$ are unclear. Several hypotheses or explanations are proposed. Hypothesis I: If the temperature signal dominates, the

seasonality of precipitation may gradually shift from DJF to SON/JJA, although this is unlikely; Hypothesis II: Temperature signals during precipitation intermissions and the dry season (in addition to precipitation events and the wet season) may also be important in determining changes of annual $\delta^{18}O_v$ and $\delta^{18}O_{ice}$; and Hypothesis III: If precipitation or the upstream moisture signal dominates, increased precipitation over the upstream areas or the local Andes may lead to depleted incoming $\delta^{18}O_v$ and/or local $\delta^{18}O_p$, though it is likely only during the mid-late Holocene.

Based on the above discussion, realistic interpretations of the tropical mountain $\delta^{18}O_{ice}$ composition during the Holocene could involve a combination of both temperature and hydroclimate signals, as no single factor can fully explain it so far. Our study highlights this challenging issue and calls for further investigation by the paleoclimate community in the future. Finally, despite the contrasting behavior between the model simulation and observations in tropical mountain $\delta^{18}O_{ice}$ during the Holocene, the likely model-data consistency in the tropical sea surface calcite $\delta^{18}O$[72] (and likely the near-surface $\delta^{18}O_v$) makes the inconsistency in the upper troposphere $\delta^{18}O_v$ even more puzzling (Fig. S6. Supplementary Notes 3).

Methods
iCESM Model and iTRACE Simulations
We use the state-of-the-art Community Earth System Model version 1.3 (iCESM) that incorporates stable water isotopes in the atmosphere, ocean, land, sea ice, and river runoff components[73]. The atmosphere component is the Community Atmosphere Model (CAM5.3)[74] and is on a 2.5° longitude and 1.9° latitude finite-volume grid with 30 hybrid vertical levels. The land component is the Community Land Model (CLM4)[75], with the same horizontal grid as the atmosphere and 10 vertical soil levels. The ocean component is the Parallel Ocean Program (POP2)[76], and the sea ice component is the Los Alamos Sea Ice Model (CECE4)[77] with nominal 1° displaced-pole grids and 60 vertical levels. The iCESM simulates the preindustrial and present-day climate well[78]. In addition, iCESM successfully captures the general observed features of precipitation isotopes in the present climate[73,79] and climate of the last deglaciation over the Asian monsoon[80], the high latitudes[81], and the tropical South American monsoon regions[82].

Using iCESM, we conducted a transient climate simulation (iTRACE) of the evolution of climate variables and water isotopes ($\delta^{18}O$ and δD) during the Holocene (11 ~ 0 ka). The Holocene simulations start from 11 ka of the previous iTRACE simulations for the last deglaciation[80] and are integrated into the present following the strategy of the previous transient simulation TRACE-21ka[83]. More details on the iTRACE setup are described in He et al.[80]. Our transient simulation incorporates water isotopes, making it feasible for a direct model-proxy data comparison on the $\delta^{18}O_{ice}$ and a comprehensive analysis of climate variability over the polar regions and tropical mountain areas. The iTRACE model has been shown to reproduce the variability of $\delta^{18}O_p$ observed in speleothem records across the Pan-Asian monsoon region[80] as well as ice core records over Greenland[81], Antarctica[84,85], and the tropical Andes[18] during the last deglaciation. Our transient simulation during the Holocene is forced by all four forcing factors, referred to as the all-forcing isotope-enabled transient climate experiment (iTRACE). The forcings include ice sheet volume and ocean bathymetry based on the ICE-6G reconstruction[86], solar insolation flux, GHG concentrations (including CO_2, CH_4, and N_2O retrieved from Lüthi et al.[87], Petit et al.[88], and Schilt et al.[89], respectively), and meltwater flux converted from the reconstructed sea-level changes, following the strategy of He et al.[80] No volcanic forcing is considered in our simulations. Aerosols, dust, and vegetation types over land are prescribed based on the PI period.

PMIP4-CMIP6 models
To understand possible forcing mechanisms of $\delta^{18}O$ over tropical mountains, we refer to the latest multi-model mid-Holoence and PI simulations provided by the Palaeoclimate Model Intercomparison Project component of the latest phase of the Coupled Model Intercomparison Project (PMIP4-CMIP6). Fourteen models are selected for analysis. The PMIP4-CMIP6 mid-Holoence simulations are driven by specified orbital forcing and a realistic atmospheric GHG concentration level at 6 ka[90]. The CO_2 concentration is ~20 ppm lower in the mid-Holocene compared to the pre-industrial (PI, 1850CE). All other forcings are the same as in PI control experiments.

Proxy system model for ice core $\delta^{18}O$
A proxy system model (PSM) is a forward model encoding mechanistic understandings of the physical and geochemical processes through which climatic information is recorded and preserved in proxy archives[71]. Integrating the ice core PSM model with the output from a climate model enables direct model-data comparison by bringing climate models into proxy space. The ice core PSM used in this study is PRYSM[16]. The input variables for the ice core PSM include annual $\delta^{18}O_p$, surface temperature, pressure, and precipitation (for calculating accumulation rate) from the iTRACE model output. A key component of the ice core PSM involves calculating the compaction and diffusion processes within the firn and solid ice. Compaction is a function of the initial density profile, which is assumed to remain fixed over time in this model. This is applicable to relatively stable climate periods without rapid climate changes (e.g., the Holocene). Annual precipitation accumulation rates are used to calculate the depth-age profile. The extent of diffusion downcore depends on permeability or density profile and is commonly described by the diffusion length, which represents the average vertical displacement of a water molecule. Meanwhile, the corresponding $\delta^{18}O_{ice}$ profile, altered by diffusion, is calculated step-wise. Further details of the ice core PSM can be found in Dee et al.[16].

We note two missing processes in this ice core PSM that may affect the direct model-data comparison. First, the total thinning of the ice core layers at each depth is not adequately accounted for. Second, the model does not incorporate diffusion in solid ice, which is driven by isotopic gradients within the lattice of the ice crystals. Both of these factors may lead to an overestimation of the low-frequency amplitude of the model $\delta^{18}O_{ice}$ in the middle and deeper sections of the ice core. Although diffusion in solid ice is much slower than diffusion in firn, the diffusion length in solid ice increases nonlinearly with rising ice temperature in the deeper parts of the core, making this effect significant and not negligible[91]. Despite the simplifications of the ice core PSM, our comparison between the model $\delta^{18}O_{ice}$ and $\delta^{18}O_p$ still shows reasonable features (Fig. S7). The high-frequency variability in $\delta^{18}O_{ice}$ is attenuated compared to that of $\delta^{18}O_p$. When the air temperature at the ice core location is similar, lower precipitation or accumulation rates lead to a larger diffusion length and, consequently, stronger smoothing of the high-frequency $\delta^{18}O_{ice}$ variability. In addition, $\delta^{18}O_p$ and $\delta^{18}O_{ice}$ exhibit a very similar long-term trend throughout the Holocene (Fig. S7), suggesting that ice core diffusion has a minimal impact on the low-frequency variability and long-term trend.

Multi-channel singular spectrum analysis
Singular Spectrum Analysis (SSA) is a nonparametric technique designed to extract meaningful information from nonlinear and noisy time series without requiring prior assumptions. Multi-channel SSA (MSSA), a natural extension of SSA, applies to time series comprising vectors or spatial maps, allowing for better consideration of correlations among multiple time series. MSSA has been widely utilized in climate science, as detailed in Ghil et al.[92]. Prior to applying MSSA, we calculate anomalies and resample the time series using a 50-year bin, ensuring that all the 11 time series have the same number of timestamps (N = 220) over the Holocene. The window size L is set to 55, satisfying the standard criterion $1 < L < N/2$. The results remain largely consistent when L is adjusted within a reasonable range. The eigenvalues derived from MSSA represent the power associated with the extracted modes. The statistical significance of each reconstruction component is evaluated using Monte Carlo methods with 1000 iterations. For each iteration, an AR(1) time series is randomly generated based on the same coefficients and variance as the original time series. A reconstruction component is statistically significant if its eigenvalue or variance

Article

contribution exceeds the 95th percentile of the eigenvalues or variance contributions obtained from the Monte Carlo experiments. Since this study focuses on long-term trends rather than high-frequency variability, the analysis focuses exclusively on the leading reconstruction component from MSSA, which captures the mode of the long-term trend and is statistically significant.

Data availability

The post-processed decadal mean iTRACE data for the Holocene simulation used in this study is available on Zenodo[93] at https://zenodo.org/records/14523565. The PMIP4-CMIP6 multi-model simulations for the PI control and mid-Holocene periods[90] are all available at https://pcmdi.llnl.gov/CMIP6/. The present-day water isotope observation data (GNIP) are available from the International Atomic Energy Agency at https://www.iaea.org/services/networks/gnip. The data necessary for reproducing figures and conducting analyses is also available on Zenodo at https://zenodo.org/records/14868857.

Code availability

The iCESM is freely available as open-source code from https://github.com/NCAR/iCESM1.2. The python code for the ice core PSM (PRYSM) is available at https://github.com/sylvia-dee/PRYSM.

References

1. Marcott, S. A., Shakun, J. D., Clark, P. U. & Mix, A. C. A reconstruction of regional and global temperature for the past 11,300 years. *science* **339**, 1198–1201 (2013).
2. Kaufman, D. S. & Broadman, E. Revisiting the Holocene global temperature conundrum. *Nature* **614**, 425–435 (2023).
3. Liu, Z. et al. The Holocene temperature conundrum. *Proc. Natl. Acad. Sci.* **111**, (2014).
4. Bader, J. et al. Global temperature modes shed light on the Holocene temperature conundrum. *Nat. Commun.* **11**, 4726 (2020).
5. Kaufman, D. et al. A global database of Holocene paleotemperature records. *Sci. Data* **7**, 1–34 (2020).
6. Bova, S., Rosenthal, Y., Liu, Z., Godad, S. P. & Yan, M. Seasonal origin of the thermal maxima at the Holocene and the last interglacial. *Nature* **589**, 548–553 (2021).
7. Cartapanis, O., Jonkers, L., Moffa-Sanchez, P., Jaccard, S. L. & De Vernal, A. Complex spatio-temporal structure of the Holocene Thermal Maximum. *Nat. Commun.* **13**, 5662 (2022).
8. Laepple, T., Shakun, J., He, F. & Marcott, S. Concerns of assuming linearity in the reconstruction of thermal maxima. *Nature* **607**, E12–E14 (2022).
9. Park, H.-S., Kim, S.-J., Stewart, A. L., Son, S.-W. & Seo, K.-H. Mid-Holocene Northern Hemisphere warming driven by Arctic amplification. *Sci. Adv.* **5**, eaax8203 (2019).
10. Thompson, A. J., Zhu, J., Poulsen, C. J., Tierney, J. E. & Skinner, C. B. Northern Hemisphere vegetation change drives a Holocene thermal maximum. *Sci. Adv.* **8**, eabj6535 (2022).
11. Hopcroft, P. O., Valdes, P. J., Shuman, B. N., Toohey, M. & Sigl, M. Relative importance of forcings and feedbacks in the Holocene temperature conundrum. *Quat. Sci. Rev.* **319**, 108322 (2023).
12. Liu, Y. et al. A Possible Role of Dust in Resolving the Holocene Temperature Conundrum. *Sci. Rep.* **8**, 4434 (2018).
13. Sigl, M., Toohey, M., McConnell, J. R., Cole-Dai, J. & Severi, M. Volcanic stratospheric sulfur injections and aerosol optical depth during the Holocene (past 11 500 years) from a bipolar ice-core array. *Earth Syst. Sci. Data* **14**, 3167–3196 (2022).
14. Osman, M. B. et al. Globally resolved surface temperatures since the Last Glacial Maximum. *Nature* **599**, 239–244 (2021).
15. Erb, M. P. et al. Reconstructing Holocene temperatures in time and space using paleoclimate data assimilation. *Clim* **18**, 2599–2629 (2022).
16. Dee, S. et al. PRYSM: An open-source framework for PRoxY System Modeling, with applications to oxygen-isotope systems. *J. Adv. Model. Earth Syst.* **7**, 1220–1247 (2015).
17. Thompson, L. G., Mosley-Thompson, E. & Henderson, K. A. Ice-core palaeoclimate records in tropical South America since the Last Glacial Maximum. *J. Quat. Sci.* **15**, 377–394 (2000).
18. Liu, Z. et al. Tropical mountain ice core δ18O: A Goldilocks indicator for global temperature change. *Sci. Adv.* **9**, eadi6725 (2023).
19. Thompson, L. G. Ice core evidence for climate change in the Tropics: implications for our future. *Quat. Sci. Rev.* **19**, 19–35 (2000).
20. Dansgaard, W. Stable isotopes in precipitation. *Tellus* **16**, 436–468 (1964).
21. Lorius, C. & Merlivat, L. *Distribution of Mean Surface Stable Isotopes Values in East Antarctica; Observed Changes with Depth in Coastal Area*. (1975).
22. Thompson, L. G. et al. A 25,000-Year Tropical Climate History from Bolivian Ice Cores. *Science* **282**, 1858–1864 (1998).
23. Thompson, L. G. et al. Late glacial stage and Holocene tropical ice core records from Huascaran, Peru. *Science* **269**, 46–50 (1995).
24. Masson-Delmotte, V. et al. Holocene climatic changes in Greenland: Different deuterium excess signals at Greenland Ice Core Project (GRIP) and NorthGRIP. *J. Geophys. Res. Atmosph.* **110**, 2004JD005575 (2005).
25. Vinther, B. M. et al. Holocene thinning of the Greenland ice sheet. *Nature* **461**, 385–388 (2009).
26. Dietrich, L. J. et al. Snow-Atmosphere Humidity Exchange at the Ice Sheet Surface Alters Annual Mean Climate Signals in Ice Core Records. *Geophys. Res. Lett.* **50**, e2023GL104249 (2023).
27. Dahl-Jensen, D. et al. Past Temperatures Directly from the Greenland Ice Sheet. *Science* **282**, 268–271 (1998).
28. Gkinis, V., Simonsen, S. B., Buchardt, S. L., White, J. W. C. & Vinther, B. M. Water isotope diffusion rates from the NorthGRIP ice core for the last 16,000 years – Glaciological and paleoclimatic implications. *Earth Planet. Sci. Lett.* **405**, 132–141 (2014).
29. Ciais, P., Jouzel, J., Petit, J. R., Lipenkov, V. & White, J. W. C. Holocene temperature variations inferred from Six Antarctic ice cores. *Ann. Glaciol.* **20**, 427–436 (1994).
30. Vimeux, F. et al. Climate variability during the last 1000 years inferred from Andean ice cores: A review of methodology and recent results. *Palaeogeogr. Palaeoclimatol. Palaeoecol.* **281**, 229–241 (2009).
31. Vuille, M. et al. Modeling δ18O in precipitation over the tropical Americas: 2. Simulation of the stable isotope signal in Andean ice cores. *J. Geophys. Res. Atmospheres* **108**, (2003).
32. Grootes, P. M., Stuiver, M., Thompson, L. G. & Mosley-Thompson, E. Oxygen isotope changes in tropical ice, Quelccaya, Peru. *J. Geophys. Res. Atmosph.* **94**, 1187–1194 (1989).
33. Aron, P. G. et al. Variability and Controls on δ18O, d-excess, and Δ′17O in Southern Peruvian Precipitation. *J. Geophys. Res. Atmospheres* **126**, e2020JD034009 (2021).
34. Kukla, T., Winnick, M. J., Laguë, M. M. & Xia, Z. The Zonal Patterns in Late Quaternary Tropical South American Precipitation. *Paleoceanogr. Paleoclimatol.* **38**, e2022PA004498 (2023).
35. Vuille, M. & Werner, M. Stable isotopes in precipitation recording South American summer monsoon and ENSO variability: observations and model results. *Clim. Dyn.* **25**, 401–413 (2005).
36. Lamantia, K., Thompson, L., Davis, M., Mosley-Thompson, E. & Stahl, H. Unique Collections of 14 C-Dated Vegetation Reveal Mid-Holocene Fluctuations of the Quelccaya Ice Cap, Peru. *J. Geophys. Res. Earth Surf.* **128**, e2023JF007297 (2023).
37. Katz, S. A. et al. Holocene Temperature and Water Stress in the Peruvian Andes: Insights From Lake Carbonate Clumped and Triple Oxygen Isotopes. *Paleoceanogr. Paleoclimatol.* **39**, e2023PA004827 (2024).

38. Stute, M. et al. Cooling of Tropical Brazil (5 °C) During the Last Glacial Maximum. *Science* **269**, 379–383 (1995).

39. Punyasena, S. W., Mayle, F. E. & McElwain, J. C. Quantitative estimates of glacial and Holocene temperature and precipitation change in lowland Amazonian Bolivia. *Geology* **36**, 667 (2008).

40. Seltzer, G., Rodbell, D. & Burns, S. Isotopic evidence for late Quaternary climatic change in tropical South America. *Geology* **28**, 35–38 (2000).

41. Ramirez, E. et al. A new Andean deep ice core from Nevado Illimani (6350 m), Bolivia. *Earth Planet. Sci. Lett.* **212**, 337–350 (2003).

42. Van Breukelen, M., Vonhof, H., Hellstrom, J., Wester, W. & Kroon, D. Fossil dripwater in stalagmites reveals Holocene temperature and rainfall variation in Amazonia. *Earth Planet. Sci. Lett.* **275**, 54–60 (2008).

43. Liu, X. & Battisti, D. S. The influence of orbital forcing of tropical insolation on the climate and isotopic composition of precipitation in South America. *J. Clim.* **28**, 4841–4862 (2015).

44. Bird, B. W., Abbott, M. B., Rodbell, D. T. & Vuille, M. Holocene tropical South American hydroclimate revealed from a decadally resolved lake sediment δ18O record. *Earth Planet. Sci. Lett.* **310**, 192–202 (2011).

45. Kanner, L. C., Burns, S. J., Cheng, H., Edwards, R. L. & Vuille, M. High-resolution variability of the South American summer monsoon over the last seven millennia: insights from a speleothem record from the central Peruvian Andes. *Quat. Sci. Rev.* **75**, 1–10 (2013).

46. Martin, K. C. et al. Greenland Ice Cores Reveal a South-To-North Difference in Holocene Thermal Maximum Timings. *Geophys. Res. Lett.* **51**, e2024GL111405 (2024).

47. He, F. & Clark, P. U. Freshwater forcing of the Atlantic Meridional Overturning Circulation revisited. *Nat. Clim. Change* **12**, 449–454 (2022).

48. Werner, M., Heimann, M. & Hoffmann, G. Isotopic composition and origin of polar precipitation in present and glacial climate simulations. *Tellus B Chem. Phys. Meteorol.* **53**, 53–71 (2001).

49. Lecavalier, B. S. et al. High Arctic Holocene temperature record from the Agassiz ice cap and Greenland ice sheet evolution. *Proc. Natl. Acad. Sci.* **114**, 5952–5957 (2017).

50. Buizert, C. et al. Greenland-Wide Seasonal Temperatures During the Last Deglaciation. *Geophys. Res. Lett.* **45**, 1905–1914 (2018).

51. Masson, V. et al. Holocene Climate Variability in Antarctica Based on 11 Ice-Core Isotopic Records. *Quat. Res.* **54**, 348–358 (2000).

52. Krinner, G., Genthon, C. & Jouzel, J. GCM analysis of local influences on ice core δ signals. *Geophys. Res. Lett.* **24**, 2825–2828 (1997).

53. Cuffey, K. M. et al. Deglacial temperature history of West Antarctica. *Proc. Natl. Acad. Sci.* **113**, 14249–14254 (2016).

54. Jones, T. R. et al. Seasonal temperatures in West Antarctica during the Holocene. *Nature* **613**, 292–297 (2023).

55. Conroy, J. L., Noone, D., Cobb, K. M., Moerman, J. W. & Konecky, B. L. Paired stable isotopologues in precipitation and vapor: A case study of the amount effect within western tropical Pacific storms. *J. Geophys. Res. Atmosph.* **121**, 3290–3303 (2016).

56. Stichler, W. et al. Influence of sublimation on stable isotope records recovered from high-altitude glaciers in the tropical Andes. *J. Geophys. Res. Atmosph.* **106**, 22613–22620 (2001).

57. Hurley, J. V., Vuille, M., Hardy, D. R., Burns, S. J. & Thompson, L. G. Cold air incursions, δ 18 O variability, and monsoon dynamics associated with snow days at Quelccaya Ice Cap, Peru. *J. Geophys. Res. Atmosph.* **120**, 7467–7487 (2015).

58. Hurley, J. V., Vuille, M. & Hardy, D. R. Forward modeling of δ 18 O in Andean ice cores. *Geophys. Res. Lett.* **43**, 8178–8188 (2016).

59. Vimeux, F. & Landais, A. The isotopic composition of the French Illimani ice core in the Bolivian Andes supports the east-west South American precipitation dipole from the last deglaciation to the mid-Holocene. *Quat. Sci. Rev.* **347**, 109098 (2025).

60. Zhao, B. et al. Tropical Andean climate variations since the last deglaciation. *Proc. Natl. Acad. Sci.* **121**, e2320143121 (2024).

61. Casado, M. et al. Archival processes of the water stable isotope signal in East Antarctic ice cores. *Cryosphere* **12**, 1745–1766 (2018).

62. Wahl, S. et al. Atmosphere-Snow Exchange Explains Surface Snow Isotope Variability. *Geophys. Res. Lett.* **49**, e2022GL099529 (2022).

63. Hardy, D. R., Vuille, M. & Bradley, R. S. Variability of snow accumulation and isotopic composition on Nevado Sajama, Bolivia. *J. Geophys. Res. Atmos.* **108**, 2003JD003623 (2003).

64. Clement, A. C., Hall, A. & Broccoli, A. The importance of precessional signals in the tropical climate. *Clim. Dyn.* **22**, 327–341 (2004).

65. Cheng, H. et al. Climate change patterns in Amazonia and biodiversity. *Nat. Commun.* **4**, 1411 (2013).

66. Rodbell, D. et al. 700,000 years of tropical Andean glaciation. *Nature* **607**, 301–306 (2022).

67. Abbott, M. B. et al. Holocene paleohydrology and glacial history of the central Andes using multiproxy lake sediment studies. *Palaeogeogr. Palaeoclimatol. Palaeoecol.* **194**, 123–138 (2003).

68. Stansell, N. D. et al. Late Glacial and Holocene glacier fluctuations at Nevado Huaguruncho in the Eastern Cordillera of the Peruvian Andes. *Geology* **43**, 747–750 (2015).

69. Smith, R. J. & Mayle, F. E. Impact of mid- to late Holocene precipitation changes on vegetation across lowland tropical South America: a paleo-data synthesis. *Quat. Res.* **89**, 134–155 (2018).

70. Victoria, A. R. L., Martinelli, L. A., Mortatti, J. & Richey, J. Mechanisms of Water Recycling in the Amazon Basin: Isotopic Insights. **20**, (1991).

71. Evans, M. N., Tolwinski-Ward, S. E., Thompson, D. M. & Anchukaitis, K. J. Applications of proxy system modeling in high resolution paleoclimatology. *Quat. Sci. Rev.* **76**, 16–28 (2013).

72. Lea, D. W. et al. Paleoclimate history of Galápagos surface waters over the last 135,000 yr. *Quat. Sci. Rev.* **25**, 1152–1167 (2006).

73. Brady, E. et al. The connected isotopic water cycle in the Community Earth System Model version 1. *J. Adv. Model. Earth Syst.* **11**, 2547–2566 (2019).

74. Neale, R. B. et al. Description of the NCAR community atmosphere model (CAM 5.0). *NCAR Tech. Note NCARTN-486 STR* **1**, 1–12 (2010).

75. Thornton, E. Technical Description of version 4.0 of the Community Land Model (CLM). *NCAR Clim. Glob.* https://doi.org/10.5065/D6FB50WZ (2010).

76. Smith, R. et al. The parallel ocean program (POP) reference manual ocean component of the community climate system model (CCSM) and community earth system model (CESM). *LAUR-01853* **141**, 1–140 (2010).

77. Hunke, E. C. Thickness sensitivities in the CICE sea ice model. *Ocean Model* **34**, 137–149 (2010).

78. Hurrell, J. W. et al. The community earth system model: a framework for collaborative research. *Bull. Am. Meteorol. Soc.* **94**, 1339–1360 (2013).

79. Nusbaumer, J., Wong, T. E., Bardeen, C. & Noone, D. Evaluating hydrological processes in the Community Atmosphere Model Version 5 (CAM5) using stable isotope ratios of water. *J. Adv. Model. Earth Syst.* **9**, 949–977 (2017).

80. He, C. et al. Hydroclimate footprint of pan-Asian monsoon water isotope during the last deglaciation. *Sci. Adv.* **7**, eabe2611 (2021).

81. He, C. et al. Abrupt Heinrich Stadial 1 cooling missing in Greenland oxygen isotopes. *Sci. Adv.* **7**, eabh1007 (2021).

82. Bao, Y., Liu, Z. & He, C. Dipole response of millennial variability in tropical South American precipitation and δ18Op during the last deglaciation: Part I: rainfall response. *J. Clim.* **36**, 4691–4707 (2023).

83. Liu, Z. et al. Transient simulation of last deglaciation with a new mechanism for Bølling-Allerød warming. *science* **325**, 310–314 (2009).

84. Buizert, C. et al. Antarctic surface temperature and elevation during the Last Glacial Maximum. *Science* **372**, 1097–1101 (2021).

85. Liu, Z. et al. Reconstruction of Past Antarctic Temperature Using Present Seasonal δ18O–Inversion Layer Temperature: Unified Slope Equations and Applications. *J. Clim.* **36**, 2933–2957 (2023).

86. Peltier, W. R., Argus, D. F. & Drummond, R. Space geodesy constrains ice age terminal deglaciation: The global ICE-6G_C (VM5a) model. *J. Geophys. Res. Solid Earth* **120**, 450–487 (2015).
87. Lüthi, D. et al. High-resolution carbon dioxide concentration record 650,000–800,000 years before present. *Nature* **453**, 379–382 (2008).
88. Petit, J. R. et al. Climate and atmospheric history of the past 420,000 years from the Vostok ice core, Antarctica. *Nature* **399**, 429–436 (1999).
89. Schilt, A. et al. Glacial–interglacial and millennial-scale variations in the atmospheric nitrous oxide concentration during the last 800,000 years. *Quat. Sci. Rev.* **29**, 182–192 (2010).
90. Otto-Bliesner, B. L. et al. The PMIP4 contribution to CMIP6–Part 2: Two interglacials, scientific objective and experimental design for Holocene and Last Interglacial simulations. *Geosci. Model Dev.* **10**, 3979–4003 (2017).
91. Holme, C., Gkinis, V. & Vinther, B. M. Molecular diffusion of stable water isotopes in polar firn as a proxy for past temperatures. *Geochim. Cosmochim. Acta* **225**, 128–145 (2018).
92. Ghil, M. et al. Advanced Spectral Methods for Climatic Time Series. *Rev. Geophys*. **40**, (2002).
93. Bao, Y., Liu, Z., Lingfeng, W. & Jiuyou, L. iTRACE-Holocene Dataset: A Holocene Transient Simulation Using the Isotope-Enabled CESM model (iCESM1.3). Zenodo https://doi.org/10.5281/zenodo.14523565 (2024).
94. Vinther, B. M. et al. Synchronizing ice cores from the Renland and Agassiz ice caps to the Greenland Ice Core Chronology. *J. Geophys. Res. Atmospheres* **113** (2008).
95. Raynaud, D. & Lorius, C. Climatic implications of total gas content in ice at Camp Century. *Nature* **243**, 283–284 (1973).
96. Vinther, B. et al. A synchronized dating of three Greenland ice cores throughout the Holocene. *J. Geophys. Res. Atmospheres* **111** (2006).
97. Fisher, D. A. et al. Penny ice cap cores, Baffin Island, Canada, and the Wisconsinan Foxe Dome connection: two states of Hudson Bay ice cover. *Science* **279**, 692–695 (1998).
98. Thompson, L. G. et al. Kilimanjaro Ice Core Records: Evidence of Holocene Climate Change in Tropical Africa. *Science* **298**, 589–593 (2002).
99. Lorius, C., Merlivat, L., Jouzel, J. & Pourchet, M. A 30,000-yr isotope climatic record from Antarctic ice. *Nature* **280**, 644–648 (1979).

Acknowledgements

Author contributions
Yuntao Bao and Zhengyu Liu conceived the study. Yuntao Bao processed data, performed the analysis and wrote the paper. Lonnie G. Thompson and Ellen Mosley-Thompson contributed to paleo proxy studies and interpretations. Lingfeng Wan and Jiuyou Lu contributed to the iTRACE simulation for the Holocene. Yuntao Bao, Zhengyu Liu, Lonnie G. Thompson, Ellen Mosley-Thompson, and Lingfeng Wan edited and reviewed the manuscript. All authors discussed the results.

Competing interests
The authors declare no competing interests.

Additional information
Supplementary information The online version contains supplementary material available at https://doi.org/10.1038/s43247-025-02188-2.

Correspondence and requests for materials should be addressed to Yuntao Bao.

Peer review information *Communications Earth & Environment* thanks the anonymous reviewers for their contribution to the peer review of this work. Primary Handling Editor: Carolina Ortiz Guerrero. A peer review file is available.

Reprints and permissions information is available at http://www.nature.com/reprints

Publisher's note Springer Nature remains neutral with regard to jurisdictional claims in published maps and institutional affiliations.